Hydrodynamic shear dissipation and transmission in lipid bilayers

Guillermo J. Amador[a,b,c], Dennis van Dijk[b], Roland Kieffer[b], Marie-Eve Aubin-Tam[b,1], and Daniel Tam[a,1]

[a]Laboratory for Aero and Hydrodynamics, Faculty of Mechanical, Maritime, and Materials Engineering, Delft University of Technology, Delft 2628 CD, The Netherlands; [b]Department of Bionanoscience, Kavli Institute of Nanoscience, Delft University of Technology, Delft 2629 HZ, The Netherlands; and [c]Experimental Zoology Group, Wageningen University & Research, Wageningen 6708 WD, The Netherlands

Vital biological processes, such as trafficking, sensing, and motility, are facilitated by cellular lipid membranes, which interact mechanically with surrounding fluids. Such lipid membranes are only a few nanometers thick and composed of a liquid crystalline structure known as the lipid bilayer. Here, we introduce an active, noncontact, two-point microrheology technique combining multiple optical tweezers probes with planar freestanding lipid bilayers accessible on both sides. We use the method to quantify both fluid slip close to the bilayer surface and transmission of fluid flow across the structure, and we use numerical simulations to determine the monolayer viscosity and the intermonolayer friction. We find that these physical properties are highly dependent on the molecular structure of the lipids in the bilayer. We compare ordered-phase with liquid disordered-phase lipid bilayers, and we find the ordered-phase bilayers to be 10 to 100 times more viscous but with 100 times less intermonolayer friction. When a local shear is applied by the optical tweezers, the ultralow intermonolayer friction results in full slip of the two leaflets relative to each other and as a consequence, no shear transmission across the membrane. Our study sheds light on the physical principles governing the transfer of shear forces by and through lipid membranes, which underpin cell behavior and homeostasis.

lipid bilayers | microfluidics | optical tweezers | membrane viscosity | intermonolayer friction

Lipid molecules self-assembled into a bilayer structure form the matrix of cell membranes (1) and enclose the entire cell as well as membrane-bound organelles. In a bilayer, lipids are aligned together, free to diffuse laterally, and experience thermal fluctuations, thus exhibiting properties akin to that of an ordered liquid crystalline sheet (2). The fluidity of the membrane is paramount to understanding cellular dynamics, as it supports membrane protein diffusion and reorganization (1). Hydrodynamic shear stresses at the interface between lipid bilayers and their aqueous environment influence the biochemical responses underlying critical functions (3), such as dictating cell shape (4), sensing (5), adhesion and locomotion (6, 7), cell division (8), and transport of molecules and ions (9–12).

The shear rheology of lipid bilayers has been investigated using passive microrheology (13–17), active microrheology with surface shear rheology (18, 19), atomic force microscopy (20), magnetically (21, 22) and optically induced fluctuation analysis (23), nanotube pulling (24, 25), fluorescence lifetime imaging of membrane-bound molecular rotors (26), and magnetic (27) and optical tweezers (28). These measurements have made use of model lipid bilayer systems including supported bilayers (29), giant unilamellar vesicles (30), Langmuir troughs (31), nanodiscs (32), and freestanding (or black) bilayers (33, 34). While these methods have contributed significantly to our understanding of lipid membranes, they often trigger out-of-plane deformation modes (e.g., out-of-plane stretching and bending), in addition to in-plane shear deformation. Many of the passive probes used are embedded within the lipid bilayer and may alter the local

physical and chemical properties (35). Furthermore, some model lipid bilayers used do not allow symmetric access to both sides of the bilayer. In such systems, the surface shear rheometry of lipid bilayers often measures the combined resistance to in-plane shear in each monolayer, characterized by the monolayer surface viscosity η_m (36) and intermonolayer friction coefficient b (22, 37), which represents the resistance to shear across the bilayer.

Here, we perform active, noncontact, two-point microrheology to characterize the viscous and frictional properties of the bilayer. Our approach uses a planar freestanding lipid bilayer (38, 39). The planar geometry of the freestanding membranes allows us to decouple in- and out-of-plane deformations, which facilitates the interpretation of the measurements using hydrodynamic models (22, 36, 37). Additionally, it enables the symmetric interfacing with double optical tweezers. Such an approach affords us the opportunity to probe both sides of the lipid bilayer symmetrically and to impose a local shear deformation both in the plane of and across the membrane. We perform two independent measurements: the drag force on a sphere translating parallel to the bilayer and the flow velocity induced on the other side of the bilayer. The first measurement allows us to quantify fluid slip in the vicinity of the membrane, while the second one characterizes the transmission of flow and shear on the other side of the bilayer. Combining these two measurements, we determine the monolayer viscosity η_m and the intermonolayer friction coefficient b from established models (37, 40). We vary the lipid

Significance

Lipid bilayers constitute the matrix of cellular membranes and synthetic vesicles used in drug delivery. This self-assembled structure is only a few nanometers thick but provides an effective barrier between aqueous fluids. The response of lipid bilayers to shear stresses induced by surrounding fluid flows can trigger biophysical processes in cells and influence the efficacy of drug delivery by synthetic vesicles. Here, we use optical tweezers to apply and measure local hydrodynamic shear stresses on both sides of a freestanding lipid bilayer. With this method, we determine the rheological properties of bilayers and capture a previously unreported phenomenon when the intermonolayer friction is so low that the monolayers slip past each other and hydrodynamic shear is not transmitted through the bilayer.

bilayer composition and provide insights into the physical roles of viscosity and friction and how they relate to lipid composition and phase.

Results

Interfacing Lipid Bilayers with Optical Tweezers. Freestanding lipid bilayers are formed in microfluidic devices following a previously described protocol (38, 39) (*Materials and Methods*). The microfluidic devices consist of two parallel rectangular microchannels (100-μm high and 500-μm wide) with several apertures between the two channels, where lipid bilayers are formed (Fig. 1*A*). The apertures extend over the entire 100-μm height of the channel and are 85-μm wide, but they decrease to 65 μm due to the swelling of the polymer during the formation of the lipid bilayer (Fig. 1 *B* and *C*). The versatility of the flow device supports the formation of lipid bilayers with different compositions, extending over the entire surface of the aperture. Here, we study membranes with two homogeneous lipid compositions, one in an ordered phase using 1,2-dipalmitoyl-*sn*-glycero-3-phosphocholine (DPPC) and one in a liquid-disordered phase using 1,2-dioleoyl-*sn*-glycero-3-phosphocholine (DOPC) (41). In addition, we also form membranes with a mixture of DOPC/DPPC with a 2:1 M ratio. The flow cells are mounted on a piezostage and placed under an inverted microscope. The surface of the membrane is parallel to the optical axis of the microscope, such that the bilayers can be interfaced with optical tweezers. The tweezers are used to trap polystyrene microspheres of radius $a = 0.5$ and 1.0 μm added to the aqueous solution. We use a double-optical trap setup using an Nd:YAG (neodymium-doped yttrium aluminum garnet; 1,064-nm wavelength) laser and measure forces on one trap using back focal plane interferometry (42). The double-trap setup supports the trapping of polystyrene microspheres on each side of the bilayer.

Drag on a Sphere in the Vicinity of a Bilayer. The shear boundary condition at the surface of a lipid bilayer has been represented using various assumptions. Such assumptions include treating the bilayer as a solid interface (43–45), an incompressible two-dimensional (2D) fluid (15, 16, 19, 36, 40), and two incompressible 2D fluids coupled by intermonolayer friction (14, 18, 22, 24, 25, 37). The nature of the boundary condition strongly influences the fluid flow in the vicinity of the bilayer. For example, the drag experienced by a translating sphere is significantly increased by the presence of a solid interface. To characterize the shear

boundary condition on a bilayer, we use measurements of the drag force on a sphere. A polystyrene bead of known radius a within a viscous fluid of viscosity μ is translated parallel to the lipid bilayer, at a prescribed velocity U relative to the bilayer. In our experiments, rather than translating the bead with the optical tweezers, we equivalently displace the membrane by moving the microfluidic device with the piezostage while keeping the bead in place with the optical tweezers (Fig. 1 *D* and *E* and Movie S1). We deduce the drag force D on the bead by measuring the bead displacement from the focal point of the optical tweezers (46) (*Materials and Methods*). Experiments are repeated at increasing distances d from the interface, $1.1a \leq d \leq 8a$.

Fig. 2*A* reports our measurements of D for a rigid glass interface (red Xs) and for bilayers of varying composition, including ordered DPPC membranes (black triangles), liquid-disordered DOPC membranes (blue circles), and DOPC/DPPC mixtures (green squares). Far from the bilayer, we find $\frac{D}{6\pi\mu Ua} \approx 1$ corresponding to the drag on a sphere in an unbounded viscous fluid. The increase in drag force D at closer distances from the bilayer strongly depends on the nature of the interface. For the solid glass interface, we observe a sharp increase in drag as $d < 3a$ (49), reaching a value of $\frac{D}{6\pi\mu Ua} = 2.4$ close to the interface at $d = 1.1a$. The drag increase close to a lipid bilayer is much more moderate and depends on the lipid composition (Fig. 2*A*). We quantify the drag increase by the ratio C_δ between the measured drag, when the bead almost touches the bilayer for $d = 1.1a$, and Stokes' drag $6\pi\mu aU$. We find values for the drag ratio coefficient ranging from $C_\delta = 1.46 \pm 0.15$ for ordered DPPC membranes to 1.12 ± 0.08 for disordered DOPC membranes. For the DOPC/DPPC membranes, we find an intermediate value of 1.21 ± 0.09.

The marked differences in drag force between the interfaces signal differences in the applicable shear boundary conditions. Interactions at a fluid–structure interface can be represented by a slip length l_s (50), which is the distance required to extrapolate the velocity profile into a rigid wall in order to obtain the same stress condition. To quantify fluid slip near the various interfaces, we introduce l_s to the prediction of drag force on a sphere near a solid interface when solving Stokes' equations as follows:

$$C_\delta = \frac{D}{6\pi\mu Ua} = \left[1 - \frac{9}{16}\frac{a}{(d+l_s)} + \frac{1}{8}\frac{a^3}{(d+l_s)^3}\right.$$
$$\left. - \frac{45}{256}\frac{a^4}{(d+l_s)^4} - \frac{1}{16}\frac{a^5}{(d+l_s)^5}\right]^{-1}. \quad \textbf{[1]}$$
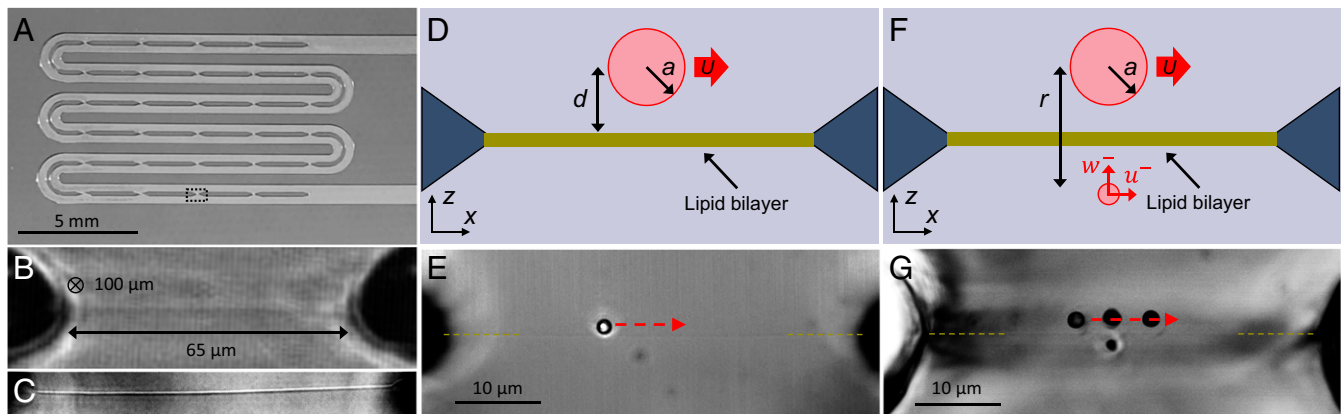

Fig. 1. Interfacing lipid bilayers with optical tweezers. (*A*) Overview of the microfluidic device used for lipid bilayer formation and optical tweezers experiments. (*B*) Close-up view of one aperture within the microfluidic device with a lipid bilayer spanning across it. (*C*) High-magnification optical image of a lipid bilayer spanning across an aperture. (*D*) Schematic and (*E*) image of the experiment for measuring the drag force. (*F*) Schematic and (*G*) overlaid image sequence of the experiment for measuring flow transmission. (*G*) The red dashed arrow represents the direction of motion. The images were captured using a light microscope and overlaid with a time step of 22 ms between images. Yellow dashed lines are used at the edges of the apertures in *E* and *G* to help visualize the bilayer. (Scale bars: *A*, 5 mm; *E* and *G*, 10 μm.)
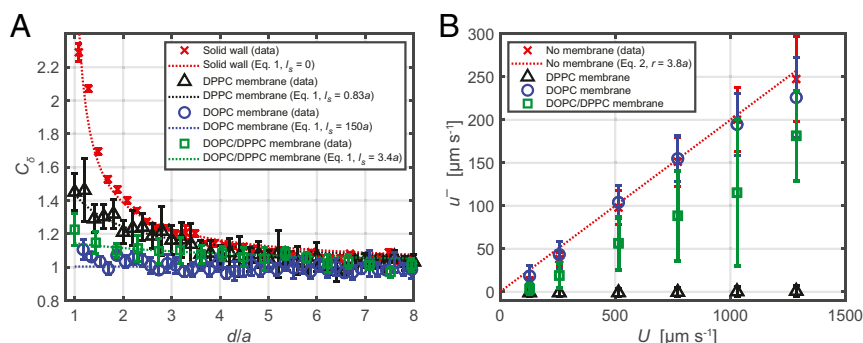
Fig. 2. Drag force and flow transmission for a sphere translating parallel to lipid bilayers. (A) Relationship between the coefficient of drag $C_\delta = \frac{D}{6\pi \mu U a}$ and the distance d from the lipid bilayer and solid glass wall. The model is from Eq. **1** (47). (B) Relationship between the flow speed u^- at a distance $r = 3.8$ μm from the moving sphere and the translation velocity U of the sphere. The model is from Eq. **2** (48). Error bars represent SDs from separate experiments performed on different membranes formed within different microfluidic devices.

For a no-slip boundary condition, the model coincides with Faxén's law (47) when $l_s = 0$, represented by the red dashed line in Fig. 2A. Our drag measurements near the solid glass interface are in agreement with a no-slip boundary condition. By fitting Eq. **1** to the measurements for each lipid type, we can determine their respective slip lengths l_s. For the ordered-phase DPPC bilayers, the slip length $l_s = 0.83a$, and the drag force is closest to that of the no-slip boundary. For the liquid disordered-phase DOPC bilayers, the slip length $l_s = 150a$, and the drag force does not increase significantly near the bilayer. For the mixed (DOPC/DPPC) bilayers, the slip length $l_s = 3.4a$, and the drag force lies between the values measured for DPPC and DOPC independently. The lipid bilayers exhibit fluid slip, as evidenced by the nonzero values of l_s, and the membranes are not accurately represented by a solid interface with the no-slip boundary condition. Our results support previous observations on lipid bilayers, where these fluid-like structures exhibit viscous (36) and frictional resistance (37), in addition to the tensile and bending resistance expected for thin films (51).

Flow Transmission and Slip across a Bilayer. We now characterize the transmission of shear stress from one side of the bilayer to the other and therefore, the interlayer interactions between the two leaflets of the bilayer. Quantifying this property requires experimental access to both sides of the bilayer. For these measurements, we use two optically trapped spheres, on each side of the bilayer (Fig. 1 F and G). We trap one sphere on one side of the bilayer and translate it, at a given velocity U parallel to the interface, in order to generate a local fluid flow in the vicinity of the bilayer. The motion of the bead is induced by deflecting the laser beam with an acousto-optic deflector, which results in the translation of the trap center. We use a second, smaller sphere on the other side of the bilayer for velocimetry (46) to measure the flow field transmitted across the bilayer (Fig. 1 F and G and Movie S2). The center to center distance between the two optical tweezers is $r = 3.8$ μm. For each lipid bilayer composition, we repeat the experiments several times using increasing values for the translation velocity $U = 100$ to 1,000 μm s^{-1} and record for each experiment the flow velocity u^- measured on the other side of the membrane.

We first report the fluid velocity u^- in the absence of a lipid bilayer, when the two beads are only separated by the aqueous phase. These measurements can be compared with Stokes' flow around a translating sphere:

$$u^- = \frac{a}{4r}\left(\frac{a^2}{r^2} + 3\right)U. \qquad [2]$$

Our measurements are in perfect agreement with the theoretical prediction from Eq. **2**, represented by the red dashed line in Fig. 2B. Strikingly, in the presence of lipid bilayers, the range of velocities u^- reported covers the extremes of what could be expected. The black triangles and blue circles are our measurements when an ordered DPPC bilayer and a disordered DOPC bilayer, respectively, are between the translating and probing spheres. For the DPPC bilayer, we measure u^- to be zero for the full range of velocity U. These measurements correspond to a complete absence of flow transmission, such that the fluid on the other side of the bilayer remains stagnant. For the liquid-disordered DOPC bilayer, we measure a significant flow transmission, with the flow velocity u^- reaching similar values as those measured when the beads are only separated by the aqueous phase and no lipid bilayer is present. The transmission of flow from one side of the bilayer to the other can be represented by the transmission coefficient C_τ, defined as the ratio between the velocity u^- measured by the probe and the velocity predicted from the Stokes' equation at the probe location. For the DPPC membranes, we find $C_\tau = 0 \pm 0.01$, while for the DOPC membranes, we find $C_\tau = 0.93 \pm 0.07$. For the DOPC/DPPC mixtures, we find partial transmission, with $C_\tau = 0.61 \pm 0.12$. Our results indicate that there is almost no slip between the monolayers of the homogeneous DOPC bilayers. Remarkably, these results suggest that there is full slip between the leaflets of the ordered DPPC bilayers and partial slip for the DOPC/DPPC mixtures.

Surface Shear Rheology. We proceed by determining the surface shear rheology of lipid bilayers, characterized by two properties: the monolayer viscosity η_m and the intermonolayer friction coefficient b. We can deduce both of these properties from the two independent measurements of the drag ratio coefficient C_δ and the flow transmission coefficient C_τ. For this purpose, we model the flow in our flow cell and in the bilayer following the classical model of Saffman (40) widely applied to flow involving lipid bilayers (19, 52). The geometry of the freestanding lipid bilayer simplifies the problem, as out-of-plane membrane deformations do not need to be taken into account. Indeed, for our observations, we find that the ratio of membrane tension to viscous forces, characterized by the capillary number, is negligible, $Ca = \frac{\mu U}{\gamma} \ll 1$, with $\gamma = 4.6 \times 10^{-6}$ N m^{-1} previously measured for a DOPC/DPPC bilayer prepared using the same method (39). Therefore, we do not expect the bilayer to deform. As such, we do not observe significant deformation of the bilayer during the experiments and assume it to remain planar in our model. The aqueous phases on each side of the membrane are modeled as two three-dimensional incompressible fluid domains of

Amador et al.
Hydrodynamic shear dissipation and transmission in lipid bilayers

PNAS | 3 of 7
https://doi.org/10.1073/pnas.2100156118

viscosity μ; $\mathbf{u}^+ = (u^+, v^+, w^+)$; and $\mathbf{u}^- = (u^-, v^-, w^-)$, satisfying the Stokes' equations, and separated by a planar interface representing the lipid bilayer (Fig. 3A). The membrane includes two planar monolayers, which we model each as a 2D incompressible fluid domain with a surface viscosity $\eta_{\mathrm{m}}/2$ (40): $\mathbf{u}_m^+ = (u_m^+, v_m^+)$ and $\mathbf{u}_m^- = (u_m^-, v_m^-)$, each satisfying the 2D Stokes' equations (Fig. 3A). Here, η_{m} represents the viscosity of the entire bilayer. The dissipative forces exerted on the membrane due to the bulk flow in the aqueous phase and due to intermonolayer friction appear as an additional interfacial stress $\boldsymbol{\sigma}$ in the 2D Stokes' equations, with $\boldsymbol{\sigma} = \mathbf{T}^+|_{z=0} \cdot \hat{\mathbf{z}} + b(\mathbf{u}_m^+ - \mathbf{u}_m^-)$, where $\hat{\mathbf{z}}$ is the unit vector in the z direction and $\mathbf{T}^+$ is the bulk hydrodynamic stress tensor (22, 37, 52). Finally, we impose a no-slip and no-penetration boundary condition at each interface between the aqueous phase and lipid bilayer (i.e., $u^\pm|_{z=0} = u_m^\pm$, $v^\pm|_{z=0} = v_m^\pm$, and $w^\pm|_{z=0} = 0$). Flow is generated through the motion of a sphere, which is treated as a solid interface. Details, including the governing equations and all boundary conditions, are provided in *SI Appendix*.

We perform the numerical simulations for a range of membrane viscosities $10^{-13} \leq \eta_{\mathrm{m}} \leq 5 \times 10^{-7}$ Pa·s·m and friction $10^{-1} \leq b \leq 10^8$ Pa·s·m^{-1} (*SI Appendix*, Fig. S2). Fig. 3 B–E represents typical flow fields obtained from our numerical simulations. Fig. 3 B and D corresponds to conditions for which no flow is transmitted, while Fig. 3 C and E corresponds to a full transmission of the flow. In Fig. 3B, the absence of flow in the aqueous phase on the opposite side of the bilayer to the moving bead is due to a velocity discontinuity across the bilayer, characteristic of a slip between the leaflets. In Fig. 3C, the velocity field is continuous across the membrane due to the near absence of slip between the leaflets and to full flow transmission. The slip between the monolayers can be visualized by representing the flow within each leaflet of the bilayer (Fig. 3 D and E).

Our numerical results are consistent with known flow regimes. We first consider the drag ratio coefficient C_δ. For large values of the membrane viscosity η_m, the bilayer has an effect on the flow similar to that of a solid membrane, and the values for C_δ approach the value of 2.4 obtained for a no-slip condition (Fig. 4A). Decreasing the membrane viscosity η_m leads to a decrease in drag C_δ. For very small values of η_m, the dissipation is mostly due to the bulk viscosity of the aqueous phase μ. In this case, a drag smaller than the Stokes' drag $C_\delta \leq 1$ is expected for small values of b, consistent with the bead being close to a free slip boundary, and a drag value close to the Stokes' drag $C_\delta \approx 1$ is expected for large values of b, when there is no slip between the two leaflets and the transmission of shear is similar to that of an equivalent aqueous layer. We consider the flow transmission next (Fig. 4B). For small values of b, there is full slip between the monolayers and $C_\tau \approx 0$. Increasing b corresponds to an increase in C_τ. It is noteworthy that C_τ is also a function of η_m since a larger membrane viscosity leads to more dissipation and therefore, to lower flow amplitudes on the other side of the bilayer. For large values of b, there is no slip between the monolayers, and the transmission C_τ decreases from one, when the membrane viscosity is negligible, to zero, when the bilayer is viscous and acts as a solid membrane.

Isocontours of C_δ and C_τ intersect for a wide range of values, and the determination of b and η_{m} requires both measurements of (C_δ, C_τ). The method is most accurate for $b = 10 - 10^4$ Pa·s·m^{-1} and $\eta_{\mathrm{m}} = 10^{-10} - 10^{-7}$ Pa·s·m. For example, we find for DOPC/DPPC mixtures, $\eta_m = 2.1 \times 10^{-9}$ Pa·s·m and $b = 600$ Pa·s·m^{-1} at the intersection between the isocontours $C_\delta = 1.2$ and $C_\tau = 0.61$ (Fig. 4C). The uncertainty on the measurements of (C_δ, C_τ) is associated with a range in the determination of (η_{m}, b), which is represented as the shaded areas in Fig. 4C. For pure DPPC, we find $8.2 \times 10^{-9} \leq \eta_{\mathrm{m}} \leq 23 \times 10^{-9}$ Pa·s·m
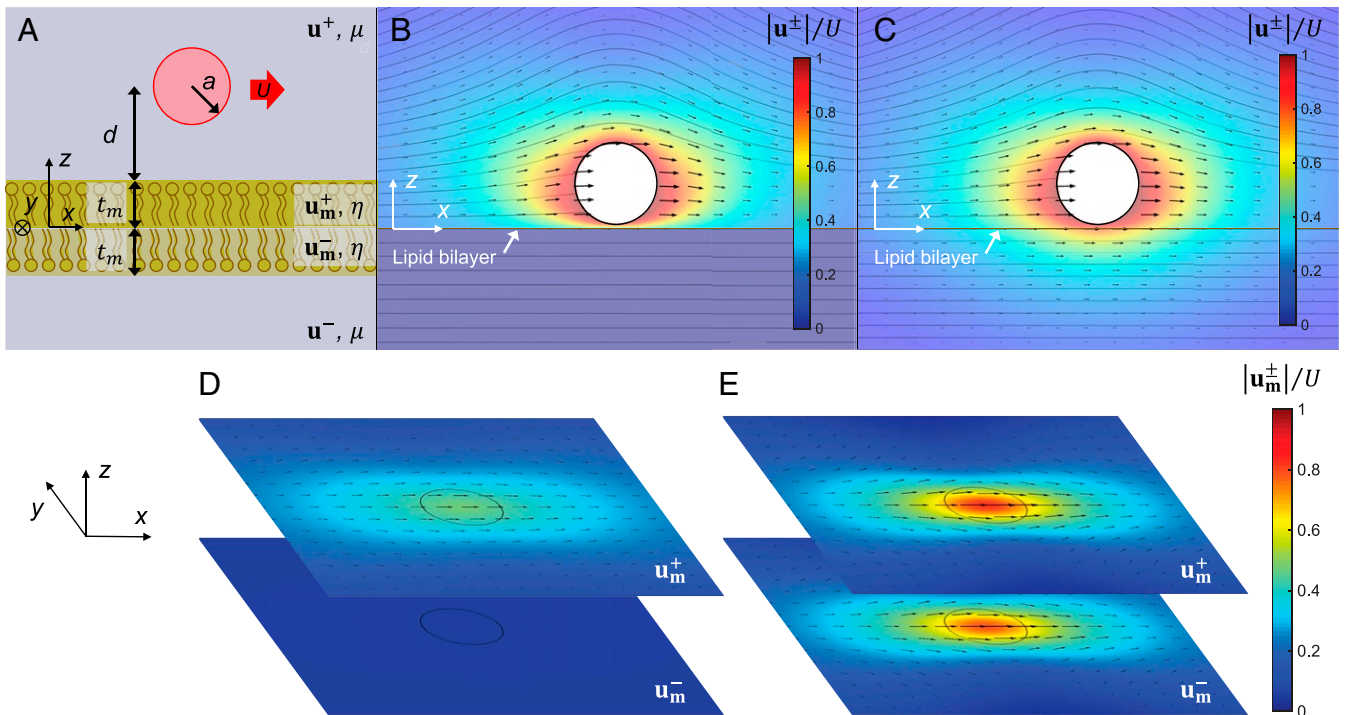

Fig. 3. Hydrodynamic model of lipid bilayers. (*A*) Schematic of the computational domain with a sphere of radius a translating parallel to a lipid bilayer of thickness $2t_m$ with a velocity U at a distance d away. The domain is split into upper aqueous $\mathbf{u}^+$, upper lipid monolayer $\mathbf{u}_m^+$, lower lipid monolayer $\mathbf{u}_m^-$, and lower aqueous $\mathbf{u}^-$. (*B* and *C*) Velocity profiles for the xz plane passing through the center of the sphere. (*D* and *E*) Velocity profiles for the xy planes coinciding with the upper $\mathbf{u}_m^+$ and lower $\mathbf{u}_m^-$ monolayers. The velocities $\mathbf{u}^\pm$ and $\mathbf{u}_m^\pm$ are normalized by the translating velocity U of the sphere. The profiles are for (*B* and *D*) $\eta_m = 2t_m\eta = 1.7 \times 10^{-8}$ Pa·s·m and $b = 3.4$ Pa·s·m^{-1} and for (*C* and *E*) $\eta_m = 1.9 \times 10^{-10}$ Pa·s·m and $b = 1.9 \times 10^4$ Pa·s·m^{-1}.
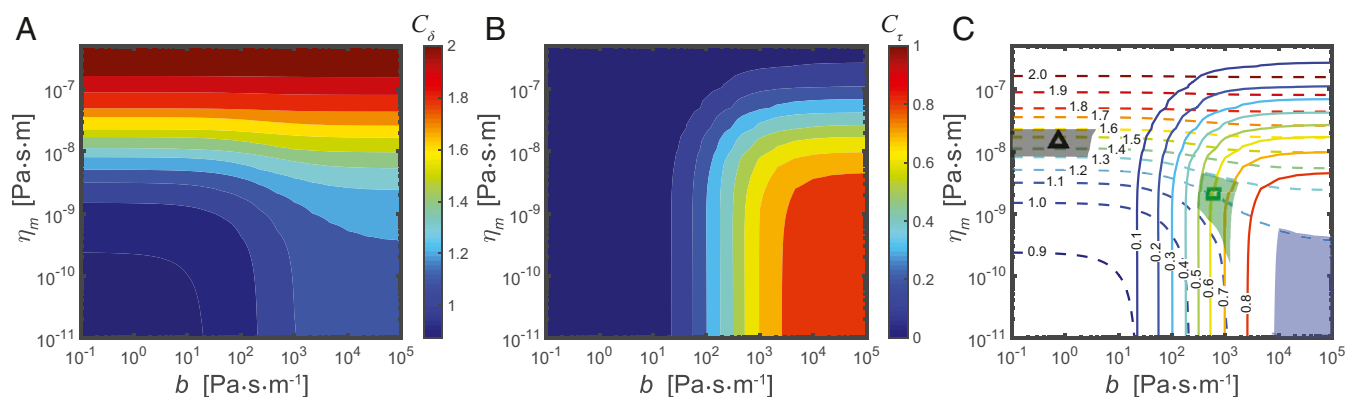
Fig. 4. Numerical simulations of drag force and flow transmission for a sphere moving parallel to lipid bilayers. Contour plots representing how (*A*) coefficient of drag C_δ and (*B*) coefficient of transmission $C_\tau = \frac{u^-}{u^-|_{r=3.8a}}$ (where $u^-|_{r=3.8a}$ is given by Eq. **2**) vary with monolayer viscosity η_m and interlayer friction b. (*C*) Isocontours of the coefficient of drag C_δ (dashed lines) and the coefficient of transmission C_τ (solid lines). The shaded regions represent the experimental values (averages and SDs from Fig. 2*A* and slopes and 95% CIs from Fig. 2*B*) for DPPC (black), DOPC (blue), and DOPC/DPPC (green).

and $b \leq 3.5$ Pa·s·m^{-1}, and for pure DOPC, $\eta_m \leq 0.6 \times 10^{-9}$ Pa·s·m and $b \geq 8 \times 10^3$ Pa·s·m^{-1}. For the DOPC/DPPC mixtures, $0.16 \times 10^{-9} \leq \eta_m \leq 4.7 \times 10^{-9}$ Pa·s·m and $0.3 \times 10^3 \leq b \leq 1.7 \times 10^3$ Pa·s·m^{-1}.

Discussion

The bilayer viscosities η_m measured with our method are in agreement with values from previous studies (14, 15, 19, 53–58). In particular, we report a viscosity of 15×10^{-9} Pa·s·m for ordered-phase DPPC membranes and 2.1×10^{-9} Pa·s·m for DOPC/DPPC mixtures, in agreement with a previous study of flow patterns inside vesicles reporting 15.9×10^{-9} Pa·s·m for liquid-ordered vesicles and 1.9×10^{-9} Pa·s·m for a comparable DOPC/DPPC mixture (19). The viscosity measured for pure DPPC membranes further agrees with measurements on DPPC liposomes obtained from the fluorescence lifetime imaging of membrane-bound molecular rotors, although our value is slightly higher (26, 59). Other studies of different mixtures have reported viscosities ranging from $2 - 6 \times 10^{-9}$ Pa·s·m (53, 54, 56–58, 60), in agreement with the viscosity we report for DOPC/DPPC mixtures. Finally, for pure DOPC bilayers, the range we deduce for the viscosity $\eta_m \leq 0.6 \times 10^{-9}$ Pa·s·m is consistent with the lower viscosities previously reported for DOPC membranes $0.16 - 0.85 \times 10^{-9}$ Pa·s·m (14, 55). It is noteworthy that for the mixture, we measure an intermediate viscosity between the values measured for the two homogeneous membranes, as has been found with other two-point microrheology approaches (60).

Fewer studies have attempted to measure the intermonolayer friction coefficients and have yielded values of $b = 1 - 50 \times 10^8$ Pa·s·m^{-1} (14, 25, 61, 62). For pure DOPC, we report full transmission of shear and close to no slip between monolayers, corresponding to a regime for which the extent of shear transmission is comparable with that of an equivalent layer of the bulk aqueous phase. In this limit, isocontours of C_τ and C_δ are almost parallel (Fig. 4*C*), and the accuracy of our method is limited. We can accurately report a lower bound $b \geq 8 \times 10^4$ Pa·s·m^{-1}, and we note that larger intermonolayer friction, on the order of 10^8 Pa·s·m^{-1}, would correspond to values of C_τ and C_δ within the error bars of our measurements and is therefore consistent with our results. For the DOPC/DPPC mixtures and the DPPC bilayers, however, we find in both cases $b \leq 10^3$, which is many orders of magnitude lower than previously reported for other lipid compositions of 1-palmitoyl-2-oleoyl-glycero-3-phosphocholine (POPC) and 1-stearoyl-2-oleoyl-sn-glycero-3-phosphocholine (SOPC) membranes (61, 62). While our values are surprisingly low, they fall within the range where our two-

point active microrheology method is the most accurate, in particular for the DOPC/DPPC mixtures. If, for example, we take as a premise the range of membrane viscosity previously reported for mixtures $2 - 6 \times 10^{-9}$ Pa·s·m, then our separate measurements of C_δ and C_τ for DOPC/DPPC membranes provide two independent estimations for b, both being consistent and smaller than 10^3 Pa·s·m^{-1}. In our study, the analysis required to fit η_m and b is greatly simplified by the planar geometry of the freestanding bilayer and does not require any assumptions on the values for the material properties of the membrane. We consider the membrane to behave as a 2D Newtonian fluid and assume a simple linear response for the intermonolayer stresses characterized by b. In previous work on freestanding bilayers, the intermonolayer friction has been estimated from the rapid relaxation times $\sim 10^{-6} - 10^{-7}$ s of shape fluctuations of wavelength smaller than 2.5 nm (61, 62). In contrast, our experimental measurements involve slower dynamics on the order of 10^{-2} s and planar geometries. It is conceivable that the interactions and overlap between the hydrocarbon chains of the two leaflets will affect the membrane dynamics differently when considering fluctuations on a length scale smaller than the size of the lipids themselves, compared with the slow shearing of a planar bilayer. The low viscosities that we measure compared with refs. 61 and 62 are a possible indication of a rate- and curvature-dependent rheology for the friction b between the monolayers, with a thickening behavior at higher rates and larger deformations. Within the shear rates that we could reach by varying U, we do not observe such thickening behavior, although we note a moderate increase of C_τ for the measurement at the highest shearing rate (Fig. 2*B*).

Conclusion

We have developed a method to characterize the shear rheology of lipid bilayers. By measuring how a lipid bilayer both dissipates (C_δ) and transmits (C_τ) hydrodynamic shear, we quantified the rheological properties of the membranes, the bilayer viscosity η_m, and intermonolayer friction b. The use of planar freestanding bilayers simplifies the analysis and modeling, such that no assumptions are required regarding the out-of-plane deformation and dynamics of the bilayer. We report measurements for three different lipid compositions in different phases and find values of membrane viscosities in agreement with previous studies. The same experiments yield extremely low values for the friction coefficient b, which indicate a significant slip between the two monolayers when an external shear flow is applied. These low values contrast with the higher ones obtained in previous studies and bespeak a rate-dependent

Amador et al.
Hydrodynamic shear dissipation and transmission in lipid bilayers

PNAS | 5 of 7
https://doi.org/10.1073/pnas.2100156118

friction rheology more complex and richer than previously assumed.

Our results highlight how the viscous and frictional properties of lipid bilayers significantly affect the transition of shear stress through the bilayer and the drag force experienced by small [$\sim$ O(1 μm)] objects in the near field. Our hydrodynamic model and experimental platform may be extended to incorporate more complexity, such as lipid mixtures, asymmetric bilayers, and embedding of other macromolecules, in order to more closely approach the in vivo conditions of cells, as well as to investigate possible nonlinear rheological behaviors of lipid bilayers.

Materials and Methods

Microfluidic Channel Fabrication. Microfluidic devices were fabricated following the technique from Marin and coworkers (38, 39). Specifically, we prepared devices with two parallel rectangular microchannels (100-μm high and 500-μm wide) with several 85-μm-wide apertures where the two channels meet and lipid bilayers can form (Fig. 1*A*). We cast the devices in Norland Optical Adhesive 81 (NOA81; Norland Products) from polydimethylsiloxane molds. The NOA81 channels were sandwiched between a microscope glass slide (Corning Incorporated; 75 $\times$ 25 mm) and a glass coverslip (Menzel-Gläzer; size: 60 $\times$ 24 mm, thickness: 170 $\pm$ 5 μm, no. 1.5). After being sealed, the microfluidic channels were functionalized using trichloro(1*H*, 1*H*, 2*H*, 2*H*-perfluorooctyl) silane (Sigma-Aldrich) at 1.5% (vol/vol) in isooctane.

Lipid Bilayer Formation. Two types of lipids were used to form the lipid bilayers, DPPC and DOPC, purchased from Avanti Lipids. For the pure compositions, the lipids were used in their stock concentrations: 10.0 mg mL^{-1} in chloroform. For the DOPC/DPPC mixture, they were mixed to a 2:1 M ratio at a 37.5-mg mL^{-1} total lipid concentration in chloroform. The bilayers were formed by first flowing the organic (chloroform) phase containing the lipids, followed by an aqueous phase. The aqueous phase consisted of 10 mM 4-(2-hydroxyethyl)-1-piperazineethanesulfonic acid (HEPES; titrated to pH 7.4 using 150 mM KCl) mixed with 0.5 mg mL^{-1} bovine serum albumin and polystyrene microspheres of radius $a' = 0.5$ and $a = 1.0$ μm (Polysciences Inc.) diluted to 1:100,000 and 1:25,000, respectively. The fluids were pushed through the microchannels using a syringe pump (ProSense NE-300) with flow rates between 0.5 and 5.0 μL min^{-1}. This technique has been shown to reproducibly form lipid bilayers that can be interfaced with optical tweezers (39). The experiments were conducted at room temperature (21 °C), where the pure lipids have been reported to be in liquid-ordered phase (DPPC) and liquid-disordered phase (DOPC) (41).

Optical Tweezers Experiments. We used optical tweezers to both measure the drag force on a particle translating near a lipid bilayer and the flow it generates on the other side of the bilayer. The methodology follows from previous studies measuring the surface tension of lipid bilayers (39) and the flow fields generated by swimming cells (63, 64). The optical tweezers used in the study are similar to those in ref. 42. Namely, an Nd:YAG laser (IPG YLR-10-LP-Y12; 1,064-nm wavelength, 10-W maximum power) was focused through a water immersion objective (Nikon CFI Plan Apo VC 60$\times$ numerical aperture [NA] = 1.20) to generate a trapping force $\mathbf{F_t} = -k\Delta\mathbf{x}$, where $\Delta\mathbf{x}$ is the bead displacement from the center of the trapping laser and k is the trap stiffness. The bead displacement $\Delta\mathbf{x}$ was measured at a sampling frequency of 50 kHz using back focal plane interferometry with a detection laser (TOPAG LDT-830-30 GC; 830-nm wavelength). The optical traps had stiffness values of $k = 0.035 - 0.083$ pN nm^{-1}. The trapped bead experiences at most 300 mW of irradiation from the lasers that may result in 3 °C of local heating (65). For a temperature difference of 3 °C, the timescale for heat transfer through diffusion is much lower than that of convection; therefore, it is insufficient to trigger convective flows.

Since the bead Reynolds number is low and inertia, added mass, and Basset forces are negligible (66), the trapping force $\mathbf{F_t}$ and hydrodynamic drag are balanced in steady state. Therefore, by measuring the trapping force, we determined the drag acting on the bead in the direction of motion, or $D = k\Delta x$. Similarly, the velocity $\mathbf{u}^- = (u^-, w^-)$ at the location of the second trapped bead (Fig. 1*C*) was determined from the measured bead displacement $\Delta\mathbf{x}$. Through a force balance between the trapping laser and hydrodynamic drag, the flow velocity in x can be expressed as $u^- = \frac{k}{6\pi\mu a'}\Delta x$.

1. S. J. Singer, G. L. Nicolson, The fluid mosaic model of the structure of cell membranes. *Science* **175**, 720–731 (1972).
2. W. H. De Jeu, B. I. Ostrovskii, A. N. Shalaginov, Structure and fluctuations of smectic membranes. *Rev. Mod. Phys.* **75**, 181 (2003).
3. A.-L. Le Roux, X. Quiroga, N. Walani, M. Arroyo, P. Roca-Cusachs, The plasma membrane as a mechanochemical transducer. *Philos. Trans. R. Soc. B* **374**, 20180221 (2019).
4. A Diz-Muñoz, O. D. Weiner, D. A. Fletcher, In pursuit of the mechanics that shape cell surfaces. *Nat. Phys.* **14**, 648 (2018).
5. O. P. Hamill, B. Martinac, Molecular basis of mechanotransduction in living cells. *Physiol. Rev.* **81**, 685–740 (2001).
6. M. P. Murrell *et al.*, Liposome adhesion generates traction stress. *Nat. Phys.* **10**, 163–169 (2014).
7. N. C. Gauthier, M. A. Fardin, P. Roca-Cusachs, M. P. Sheetz, Temporary increase in plasma membrane tension coordinates the activation of exocytosis and contraction during cell spreading. *Proc. Natl. Acad. Sci. U.S.A.* **108**, 14467–14472 (2011).
8. J. A. Lucy, The fusion of biological membranes. *Nature* **227**, 815–817 (1970).
9. B.-T. Pan, K. Teng, C. Wu, M. Adam, R. M. Johnstone, Electron microscopic evidence for externalization of the transferrin receptor in vesicular form in sheep reticulocytes. *J. Cell Biol.* **101**, 942–948 (1985).
10. R. M. Johnstone, M. Adam, J. R. Hammond, L. Orr, Claire. Turbide, Vesicle formation during reticulocyte maturation. association of plasma membrane activities with released vesicles (exosomes). *J. Biol. Chem.* **262**, 9412–9420 (1987).
11. I. Mellman, Endocytosis and molecular sorting. *Annu. Rev. Cell Dev. Biol.* **12**, 575–625 (1996).
12. A. Rustom, R. Saffrich, I. Markovic, P. Walther, H.-H. Gerdes, Nanotubular highways for intercellular organelle transport. *Science* **303**, 1007–1010 (2004).
13. R. Peters, R. J. Cherry, Lateral and rotational diffusion of bacteriorhodopsin in lipid bilayers: Experimental test of the Saffman-Delbrück equations. *Proc. Natl. Acad. Sci. U.S.A.* **79**, 4317–4321 (1982).
14. R. Merkel, E. Sackmann, E. Evans, Molecular friction and epitactic coupling between monolayers in supported bilayers. *J. Phys.* **50**, 1535–1555 (1989).
15. R. Dimova, C. Dietrich, A. Hadjiisky, K. Danov, B. Pouligny, Falling ball viscosimetry of giant vesicle membranes: Finite-size effects. *Euro. Phys. J. B Condens. Matter Complex Syst.* **12**, 589–598 (1999).
16. P. Cicuta, S. L. Keller, S. L. Veatch, Diffusion of liquid domains in lipid bilayer membranes. *J. Phys. Chem. B* **111**, 3328–3331 (2007).
17. R. Shlomovitz, A. A. Evans, T. Boatwright, M. Dennin, A. J. Levine, Measurement of monolayer viscosity using noncontact microrheology. *Phys. Rev. Lett.* **110**, 137802 (2013).
18. P. Jonsson, J. P. Beech, J. O. Tegenfeldt, F. Hook, Mechanical behavior of a supported lipid bilayer under external shear forces. *Langmuir* **25**, 6279–6286 (2009).
19. A. R. Honerkamp-Smith, F. G. Woodhouse, V. Kantsler, R. E. Goldstein, Membrane viscosity determined from shear-driven flow in giant vesicles. *Phys. Rev. Lett.* **111**, 038103 (2013).
20. Z. Al-Rekabi, S. Contera, Multifrequency AFM reveals lipid membrane mechanical properties and the effect of cholesterol in modulating viscoelasticity. *Proc. Natl. Acad. Sci. U.S.A.* **115**, 2658–2663 (2018).
21. W. Pfeiffer, S. König, J. F. Legrand, T. Bayerl, D. Richter, E. Sackmann, Neutron spin echo study of membrane undulations in lipid multibilayers. *Europhys. Lett.* **23**, 457 (1993).
22. U. Seifert, S. A. Langer, Viscous modes of fluid bilayer membranes. *Europhys. Lett.* **23**, 71 (1993).
23. J. S. Lum, J. D. Dove, T. W. Murray, M. A. Borden, Single microbubble measurements of lipid monolayer viscoelastic properties for small-amplitude oscillations. *Langmuir* **32**, 9410–9417 (2016).
24. E. Evans, A. Yeung, Hidden dynamics in rapid changes of bilayer shape. *Chem. Phys. Lipids* **73**, 39–56 (1994).
25. R. M. Raphael, R. E. Waugh, Accelerated interleaflet transport of phosphatidylcholine molecules in membranes under deformation. *Biophys. J.* **71**, 1374–1388 (1996).
26. Y. Wu *et al.*, Molecular rheometry: Direct determination of viscosity in l o and l d lipid phases via fluorescence lifetime imaging. *Phys. Chem. Chem. Phys.* **15**, 14986–14993 (2013).
27. K. H. Kim, S. Q. Choi, J. A. Zasadzinski, T. M. Squires, Interfacial microrheology of DPPC monolayers at the air–water interface. *Soft Matter* **7**, 7782–7789 (2011).

6 of 7 | PNAS
https://doi.org/10.1073/pnas.2100156118

Amador et al.
Hydrodynamic shear dissipation and transmission in lipid bilayers

28. S.-H. Wu *et al.*, Viscoelastic deformation of lipid bilayer vesicles. *Soft Matter* **11**, 7385–7391 (2015).

29. E. Sackmann, Supported membranes: Scientific and practical applications. *Science* **271**, 43–48 (1996).

30. A. D. Bangham, M. M. Standish, J. C. Watkins, Diffusion of univalent ions across the lamellae of swollen phospholipids. *J. Mol. Biol.* **13**, 238–IN27 (1965).

31. D. A. Cadenhead, F. Muller-Landau, B. M. J. Kellner, Bilayers at the air—water interface? *Nature* **252**, 694–696 (1974).

32. T. H. Bayburt, Y. V Grinkova, S. G. Sligar, Self-assembly of discoidal phospholipid bilayer nanoparticles with membrane scaffold proteins. *Nano Lett.* **2**, 853–856 (2002).

33. P. Mueller, D. O. Rudin, H. T. Tien, W. C. Wescott, Reconstitution of cell membrane structure in vitro and its transformation into an excitable system. *Nature* **194**, 979–980 (1962).

34. M. Montal, P. Mueller, Formation of bimolecular membranes from lipid monolayers and a study of their electrical properties. *Proc. Natl. Acad. Sci. U.S.A.* **69**, 3561–3566 (1972).

35. T. M. Squires, Nonlinear microrheology: Bulk stresses versus direct interactions. *Langmuir* **24**, 1147–1159 (2008).

36. P. G. Saffman, M. Delbrück, Brownian motion in biological membranes. *Proc. Natl. Acad. Sci. U.S.A.* **72**, 3111–3113 (1975).

37. E. Evans, E. Sackmann, Translational and rotational drag coefficients for a disk moving in a liquid membrane associated with a rigid substrate. *J. Fluid Mech.* **194**, 553–561 (1988).

38. V. Marin, R. Kieffer, R. Padmos, M.-E. Aubin-Tam, Stable free-standing lipid bilayer membranes in Norland optical adhesive 81 microchannels. *Anal. Chem.* **88**, 7466–7470 (2016).

39. A. Dols-Perez *et al.*, Artificial cell membranes interfaced with optical tweezers: A versatile microfluidics platform for nanomanipulation and mechanical characterization. *ACS Appl. Mater. Interfaces* **11**, 33620–33627 (2019).

40. P. G. Saffman, Brownian motion in thin sheets of viscous fluid. *J. Fluid Mech.* **73**, 593–602 (1976).

41. Z. V. Leonenko, E. Finot, H. Ma, T. E. S. Dahms, D. T. Cramb, Investigation of temperature-induced phase transitions in DOPC and DPPC phospholipid bilayers using temperature-controlled scanning force microscopy. *Biophys. J.* **86**, 3783–3793 (2004).

42. M. J. Lang, C. L. Asbury, J. W. Shaevitz, S. M. Block, An automated two-dimensional optical force clamp for single molecule studies. *Biophys. J.* **83**, 491–501 (2002).

43. S. M. Johnson, A. D. Bangham, M. W. Hill, E. D. Korn, Single bilayer liposomes. *Biochim. Biophys. Acta* **223**, 820–826 (1971).

44. J. T. Mason, C. Huang, Hydrodynamic analysis of egg phosphatidylcholine vesicles. *Ann. N. Y. Acad. Sci.* **308**, 29–48 (1978).

45. S. R. Tabaei, J. J. J. Gillissen, S. Block, F. Höök, N.-J. Cho, Hydrodynamic propulsion of liposomes electrostatically attracted to a lipid membrane reveals size-dependent conformational changes. *ACS Nano* **10**, 8812–8820 (2016).

46. P. G. Dehnavi, D. Wei, M.-E. Aubin-Tam, D. S. W. Tam, Optical tweezers-based velocimetry: A method to measure microscale unsteady flows. *Exp. Fluid* **61**, 1–15 (2020).

47. H. Faxén, Der widerstand gegen die bewegung einer starren kugel in einer zähen flüssigkeit, die zwischen zwei parallelen ebenen wänden eingeschlossen ist. *Ann. Phys.* **373**, 89–119 (1922).

48. J. Happel, H. Brenner, *Low Reynolds Number Hydrodynamics* (Mrtinus Nijhoff Publishers, 1963), vol. 1.

49. E. Schäffer, S. F. Nørrelykke, J. Howard, Surface forces and drag coefficients of microspheres near a plane surface measured with optical tweezers. *Langmuir* **23**, 3654–3665 (2007).

50. L. Bocquet, J.-L. Barrat, Flow boundary conditions from nano-to micro-scales. *Soft Matter* **3**, 685–693 (2007).

51. B. Rallabandi, N. Oppenheimer, M. Y. B. Zion, H. A. Stone, Membrane-induced hydroelastic migration of a particle surfing its own wave. *Nat. Phys.* **14**, 1211–1215 (2018).

52. J. T. Schwalbe, P. M. Vlahovska, M. J. Miksis, Monolayer slip effects on the dynamics of a lipid bilayer vesicle in a viscous flow. *J. Fluid Mech.* **647**, 403–419 (2010).

53. E. P. Petrov, P. Schwille, Translational diffusion in lipid membranes beyond the Saffman-Delbrück approximation. *Biophys. J.* **94**, L41–L43 (2008).

54. B. A. Camley, C. Esposito, T. Baumgart, F. L. H. Brown, Lipid bilayer domain fluctuations as a probe of membrane viscosity. *Biophys. J.* **99**, L44–L46 (2010).

55. C. Herold, P. Schwille, E. P. Petrov, DNA condensation at freestanding cationic lipid bilayers. *Phys. Rev. Lett.* **104**, 148102 (2010).

56. E. P. Petrov, R. Petrosyan, P. Schwille, Translational and rotational diffusion of micrometer-sized solid domains in lipid membranes. *Soft Matter* **8**, 7552–7555 (2012).

57. A. R. Honerkamp-Smith, B. B. Machta, S. L. Keller. Experimental observations of dynamic critical phenomena in a lipid membrane. *Phys. Rev. Lett.* **108**, 265702 (2012).

58. C. A. Stanich *et al.*, Coarsening dynamics of domains in lipid membranes. *Biophys. J.* **105**, 444–454 (2013).

59. Y. Nojima, K. Iwata, Viscosity heterogeneity inside lipid bilayers of single-component phosphatidylcholine liposomes observed with picosecond time-resolved fluorescence spectroscopy. *J. Phys. Chem. B* **118**, 8631–8641 (2014).

60. T. T. Hormel, M. A. Reyer, R. Parthasarathy, Two-point microrheology of phase-separated domains in lipid bilayers. *Biophys. J.* **109**, 732–736 (2015).

61. T. Pott, P. Méléard, The dynamics of vesicle thermal fluctuations is controlled by intermonolayer friction. *Europhys. Lett.* **59**, 87 (2002).

62. L. R. Arriaga *et al.*, Dissipative curvature fluctuations in bilayer vesicles: Coexistence of pure-bending and hybrid curvature-compression modes. *Euro. Phys. J. E* **31**, 105–113 (2010).

63. D. Wei, P. G. Dehnavi, M.-E. Aubin-Tam, D. Tam, Is the zero Reynolds number approximation valid for ciliary flows? *Phys. Rev. Lett.* **122**, 124502 (2019).

64. G. J. Amador, D. Wei, D. Tam, M.-E. Aubin-Tam, Fibrous flagellar hairs of *Chlamydomonas reinhardtii* do not enhance swimming. *Biophys. J.* **118**, 2914–2925 (2020).

65. K. C. Neuman, A. Nagy, Single-molecule force spectroscopy: Optical tweezers, magnetic tweezers and atomic force microscopy. *Nat. Methods* **5**, 491–505 (2008).

66. S. Kim, S. J. Karrila, *Microhydrodynamics: Principles and Selected Applications* (Dover Publications, Mineola, NY, 2013).

67. G. J. Amador, D. van Dijk, R. Kieffer, M.-E. Aubin-Tam, D. Tam, Data underlying the publication: Hydrodynamic shear dissipation and transmission in lipid bilayers. 4TU.ResearchData Repository. https://data.4tu.nl/articles/dataset/Data_underlying_the_publication_Hydrodynamic_shear_dissipation_and_transmission_in_lipid_bilayers/14472705. Deposited 23 April 2021.

Amador et al.
Hydrodynamic shear dissipation and transmission in lipid bilayers

PNAS | 7 of 7
https://doi.org/10.1073/pnas.2100156118